Sand ripples under sea waves. Part 4. Tile ripple formation

By P. C. ROOS[1,2] and P. BLONDEAUX[1]

[1]Department of Environmental Engineering, University of Genova, Via Montallegro, 1, 16145 Genova, Italy

[2]Department of Civil Engineering, University of Twente, P.O. Box 217, 7500 AE Enschede, The Netherlands

We investigate the formation of small-scale three-dimensional bedforms due to interactions of an erodible bed with a sea wave that obliquely approaches the coast, being partially reflected at the beach. In this case the trajectories of fluid particles at the top of the bottom boundary layer are ellipses in the horizontal plane, the axes of which depend on the angle of wave incidence and the distance from the shore. A weakly nonlinear stability analysis of an initially flat, cohesionless, sandy bottom is performed. We focus on the resonant interaction of three perturbation components. The results show that these elliptical forcing conditions are responsible for the formation of both brick-pattern ripples and tile ripples. In particular tile ripples are associated with a flow at the top of the bottom boundary layer which is near-circular (ellipticity close to one), whereas brick-pattern ripples are related to a unidirectional oscillatory flow (zero ellipticity).

1. Introduction

Occasionally, underneath sea waves, small three-dimensional bedforms (ripples) are observed which consist of sets of crests arranged in different patterns. Sometimes the overall bottom configuration turns out to be amazingly regular. In particular bottom topography may resemble bricks or tiles arranged to form regular patterns (see figure 1). Both the existence of brick-pattern ripples and tile ripples seem to express complex bed–fluid interactions.

A first attempt to explain the mechanism leading to the appearance of three-dimensional ripples, and in particular of brick-pattern ripples, has been made by Hara & Mei (1990) who investigated the stability of the Stokes layer induced by a sea wave over two-dimensional ripples with respect to spanwise perturbations. In some cases the flow which is set up by the growth of the perturbations could be either harmonic (periodic within one wavelength of the ripples) or subharmonic (periodic within twice the wavelength of ripples) depending on the mode of instability. The associated steady streaming along the ripple surface shows a tendency to accumulate sand particles in various patterns, including one suggesting the initiation of brick-pattern ripples. In this case the growth of transverse perturbations is due to a Taylor–Görtler instability induced by the centrifugal effects associated with the curvature of the streamlines of the basic oscillatory flow over the two-dimensional wavy bottom.

A different mechanism has been suggested by Vittori & Blondeaux (1992) who showed that brick-pattern ripples can be generated by the simultaneous growth of
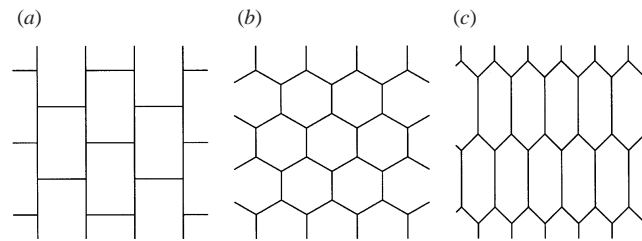
(*a*)   (*b*)   (*c*)

FIGURE 1. Sketch of wave related ripples in terms of crest lines in plan, taken from Allen (1984): (*a*) brick-pattern ripples, (*b*) equant hexagonal tile ripples, (*c*) inequant hexagonal tile ripples.

two-dimensional and three-dimensional bottom perturbations which interact with each other through a mechanism similar to that described by Craik (1971) in a different context.

Both in Hara & Mei (1990) and in Vittori & Blondeaux (1992), a basic unidirectional oscillatory flow is considered and fluid particles at the top of the bottom boundary layer oscillate to and fro. However when a progressive wave, propagating on water of uniform depth, obliquely approaches the coast and is partially reflected at the beach, a complex wave field is generated and the surface elevation is periodic both in the cross-shore and in the longshore directions. At a fixed location, close to the sea bed, the irrotational flow drives a horizontal orbital motion which can be described by an ellipse in a horizontal plane, the axes of which depend on the amplitudes and the directions of the incident and reflected waves and on the particular chosen cross-shore location (Roos 2000). In other words, at the top of the bottom boundary layer the oscillating flow is not unidirectional but the velocity has two components which oscillate with the same angular frequency, with different amplitudes and a phase shift of $\pi/2$.

Even though there is a considerable amount of literature devoted to the study of bedforms generated by unidirectional oscillatory flows and in particular of ripples, the investigation of bed topography induced by complex flows is still incomplete. Silvester (1972, 1975) roughly described sand ripple formation under the action of waves obliquely reflected from a vertical wall. Qualitative information is also given by Irie & Nadaoka (1984) and Hsu, Silvester & Tsuchiya (1980). More recently, the experimental work by Jan & Lin (1998) suggests a direct relation between the ellipticity of the flow just outside the boundary layer and the presence of bedforms with different characteristics. Jan & Lin (1998) studied the bedforms triggered by a wave field generated by an oblique standing wave resulting from obliquely incident waves fully reflecting from a vertical wall. In particular, at offshore locations where the oscillatory flow outside the bottom boundary layer is unidirectional oscillatory (in either the longshore or the cross-shore direction) they observed two-dimensional ripples with crests perpendicular to the direction of the oscillatory flow. Hence the ripples have crests aligned perpendicular to the wall under the antinodes of the oblique standing wave, whereas ripple crests are aligned with the wall and ride on the top of large-scale sandbars under the nodes. At offshore locations, where the flow is not unidirectional oscillatory but elliptical or even circular, Jan & Lin (1998) observed three-dimensional bedforms, which they refer to as 'island' ripples of a honeycombed structure.

The present work is devoted to the study of ripple formation when the flow just outside the bottom boundary layer is elliptical. One of the aims of the work is the investigation of ripple characteristics on varying the ellipse describing fluid

displacement at the top of the boundary layer. In particular we investigate whether brick-pattern ripples, tile ripples and other three-dimensional ripples are originated by different physical mechanisms or whether they are simply the result of the growth of three-dimensional bottom perturbations driven by the same mechanism when the parameters of the problem assume different values.

The present work is a continuation of the research carried out by Blondeaux (1990), Vittori & Blondeaux (1990, 1992) and Blondeaux, Foti & Vittori (2000).

The procedure used in the rest of the paper is the following. In the next section we formulate the problem. Next, in §3, bottom perturbations of small amplitude are considered and a linear analysis is carried out. The nonlinear interaction between different perturbation components is studied in §4 and the results are presented in both §5 and §6. Finally the relevance of the theory in explaining both brick-pattern and tile ripples is discussed in §7.

2. Formulation of the problem and basic state

Let us consider two waves, both of angular frequency ω^*, but characterized by different small amplitudes a_1^* and a_2^* and propagating along two different directions forming an arbitrary angle β (herein a star denotes a dimensional quantity). By using the linear Stokes theory to describe the flow outside the bottom boundary layer, it can be easily verified that the velocity close to the bottom is described by

$$(u^*, v^*, w^*) = (-U_0^* \cos \omega^* t^*, 0, -W_0^* \sin \omega^* t^*), \tag{2.1}$$

where (u^*, v^*, w^*) are the velocity components along the three axes of a Cartesian co-ordinate system with the y^*-axis vertical and pointing upwards and the (x^*, z^*)-plane coincident with the bottom. The amplitudes U_0^*, W_0^* of the velocity oscillations along the x^*- and z^*-axes are related to a_1^*, a_2^*, β and the local water depth h_0^* (Roos 2000). If attention is focused on a region of the same order of magnitude as the thickness δ^* of the bottom boundary layer and if δ^* is assumed to be much smaller than h_0^* and L^* (the length of the sea waves), the spatial dependence of U_0^* and W_0^* can be assumed to be negligible. If the bottom is flat, the flow inside the bottom boundary layer can be easily determined (see e.g. Mei 1989) and using a complex notation, it is

$$v_0^* = (u_0^*, v_0^*, w_0^*) = \frac{U_0^*}{2} [e^{-(1+i)y^*/\delta^*} - 1] e^{i\omega^* t^*} (1, 0, -i\sigma) + \text{c.c.}, \tag{2.2}$$

where δ^* is equal to $(2v^*/\omega^*)^{1/2}$, v^* being the kinematic viscosity of the sea water. Moreover, we have introduced an ellipticity parameter $\sigma \equiv W_0^*/U_0^*$ and c.c. denotes the complex conjugate of a complex number. When the bottom is cohesionless and formed by sediment of uniform size d^*, density ρ_s^* and porosity n, quite often bedforms (ripples) appear. In order to investigate the process leading to the formation of ripples, let us introduce a perturbation of the flat bottom configuration and determine its time development.

If the perturbation is assumed to be of small amplitude (strictly infinitesimal), the problem can be linearized and the generic component can be considered:

$$y^* = \eta^*(x^*, z^*, t^*) = \epsilon^* C(t^*) e^{i(\alpha^* x^* + \gamma^* z^*)} + \text{c.c.} \tag{2.3}$$

where α^* and γ^* denote the perturbation wavenumbers in the x^*- and z^*-directions, respectively, and the amplitude $\epsilon^* C(t^*)$ depends on time. Moreover ϵ^* is assumed to be much smaller than δ^* and $C(t^*)$ to be of order one. To determine the time development of the bottom configuration it is necessary to solve the morphodynamic problem posed

by the Navier–Stokes equations, fluid continuity and sediment continuity equations and a relationship between fluid and sediment motions. Introducing the following dimensionless variables:

$$(x, y, z) \equiv (x^*, y^*, z^*)/\delta^*, \quad t \equiv t^*\omega^*, \quad \epsilon \equiv \epsilon^*/\delta^*, \quad \eta \equiv \eta^*/\delta^*,$$
$$(\alpha, \gamma) \equiv (\alpha^*, \gamma^*)\delta^*, \quad \boldsymbol{v} \equiv (u, v, w) \equiv (u^*, v^*, w^*)/U_0^*, \qquad \qquad (2.4)$$
$$p \equiv p^*/\rho U_0^{*2}, \quad \boldsymbol{q} \equiv (q_x, q_z) \equiv \boldsymbol{q}^*/\sqrt{(s-1)g^* d^{*3}}$$

(where p^* is pressure, $\boldsymbol{q}^* \equiv (q_x^*, q_z^*)$ denote the sediment transport rate per unit width in the x^*- and z^*-directions, respectively, $s = \rho_s^*/\rho^*$ is the ratio between sediment and fluid densities and g^* the gravitational acceleration), the problem is

$$\frac{2}{R_\delta}\frac{\partial \boldsymbol{v}}{\partial t} + \boldsymbol{v} \cdot \nabla \boldsymbol{v} = -\nabla p + \frac{1}{R_\delta}\nabla^2 \boldsymbol{v}, \qquad (2.5a)$$

$$\nabla \cdot \boldsymbol{v} = 0, \qquad (2.5b)$$

$$\frac{2\Psi^{1/2}}{R_d}(1-n)\frac{\partial \eta}{\partial t} + \nabla \cdot \boldsymbol{q} = 0, \qquad (2.5c)$$

$$\boldsymbol{q} = a \left| \frac{2}{R_d}V - \frac{\mu}{\Psi}\nabla\eta \right|^{b-1} \left(\frac{2}{R_d}V - \frac{\mu}{\Psi}\nabla\eta \right), \qquad (2.5d)$$

where $V = (u, w)$ is (the horizontal projection of) the velocity vector evaluated at half a grain diameter above the bed, i.e. at $y^* = \eta^* + \frac{1}{2}d^*$. To quantify the sediment transport rate $\boldsymbol{q}^*$, a simple relationship is used relating $\boldsymbol{q}^*$ to the agitating forces which act on sediment grains. As discussed in Blondeaux (1990) and Blondeaux *et al.* (2000), the sediment transport rate can be assumed to be proportional to some power b of the agitating forces (drag and gravity forces). Here the drag force is assumed proportional to $\rho^* v^* V^* d^*$ and the gravity component along the bed profile to $(\rho_s^* - \rho^*)g^* d^{*3}\nabla\eta^*$. In (2.5) the following dimensionless numbers appear:

$$R_\delta \equiv \frac{U_0^*\delta^*}{v^*}, \quad R_d \equiv \frac{U_0^* d^*}{v^*}, \quad \Psi \equiv \frac{U_0^{*2}}{(s-1)g^* d^*}, \qquad (2.6)$$

which are the flow Reynolds number, the sediment Reynolds number and the sediment mobility number, respectively. Moreover the values of the constants appearing in (2.5c, d) and (2.6) are

$$a = 1.23\frac{s-1}{s}\Psi^{3.36}R_d^{1.83}, \quad b = 4.28, \quad \mu = 0.15, \quad s = 2.65, \quad n = 0.45. \qquad (2.7)$$

The values of a and b have been estimated in the relevant range of the parameters by requiring that relationship (2.5d) should match the empirical law proposed by Grass & Ayoub (1982) when the ratio d^*/δ^* tends to zero. The constant μ, introduced by Fredsøe (1974) who suggested a value ranging between 0.1 and 1, has been given the value 0.15 used by Blondeaux (1990). Finally the values of s and n are those characteristic of sand.

In order to close the problem, boundary conditions need to be specified. At the bottom, the no-slip condition should be forced while for y^* much larger than δ^*, i.e. for y tending to infinity, the velocity should be matched with (2.1):

$$\boldsymbol{v}|_{y=\eta} = \boldsymbol{0}, \quad \lim_{y\to\infty} \boldsymbol{v} = -(\cos t, 0, \sigma \sin t). \qquad (2.8)$$

As previously pointed out, the quantity ϵ is assumed to be much smaller than one.

Therefore, the solution can be expanded in terms of ϵ:

$$v = v_0(y,t) + \epsilon C(t)v_1(y,t)e^{i(\alpha x + \gamma z)} + \text{c.c.} + O(\epsilon^2), \qquad (2.9a)$$

$$p = p_0(x,z,t) + \epsilon C(t)p_1(y,t)e^{i(\alpha x + \gamma z)} + \text{c.c.} + O(\epsilon^2), \qquad (2.9b)$$

$$q = q_0(t) + \epsilon C(t)q_1(t)e^{i(\alpha x + \gamma z)} + \text{c.c.} + O(\epsilon^2). \qquad (2.9c)$$

At the leading order of approximation bed variations are absent (see (2.3)) and the flow field can be easily determined and in dimensionless form it is

$$v_0 = (u_0, v_0, w_0) = \tfrac{1}{2}[e^{-(1+i)y} - 1]e^{it}(1, 0, -i\sigma) + \text{c.c.} \qquad (2.10)$$

The fluid trajectories of the basic flow describe ellipses of eccentricity σ at every point in the bottom boundary layer. The sediment follows elliptical paths, as well, and the bed remains flat since the horizontal divergences of the sediment transport vanish.

3. The perturbations

At order ϵ the following linear problem for u_1, v_1, w_1, p_1 and q_{x1}, q_{z1} is found:

$$\frac{2}{R_\delta}\frac{\partial u_1}{\partial t} + i\alpha u_0 u_1 + v_1 \frac{\partial u_0}{\partial y} + i\gamma w_0 u_1 = -i\alpha p_1 + \frac{1}{R_\delta}N^2 u_1, \qquad (3.1a)$$

$$\frac{2}{R_\delta}\frac{\partial v_1}{\partial t} + i\alpha u_0 v_1 + i\gamma w_0 v_1 = -\frac{\partial p_1}{\partial y} + \frac{1}{R_\delta}N^2 v_1, \qquad (3.1b)$$

$$\frac{2}{R_\delta}\frac{\partial w_1}{\partial t} + i\alpha u_0 w_1 + v_1 \frac{\partial w_0}{\partial y} + i\gamma w_0 w_1 = -i\gamma p_1 + \frac{1}{R_\delta}N^2 w_1, \qquad (3.1c)$$

$$i\alpha u_1 + \frac{\partial v_1}{\partial y} + i\gamma w_1 = 0, \qquad (3.1d)$$

$$\frac{2\Psi^{1/2}}{R_d}(1-n)\frac{\mathrm{d}C(t)}{\mathrm{d}t} + (i\alpha q_{x1} + i\gamma q_{z1})C(t) = 0, \qquad (3.1e)$$

$$(u_1, v_1, w_1) + \left(\frac{\partial u_0}{\partial y}, 0, \frac{\partial w_0}{\partial y}\right)\bigg|_{y=0} = 0, \qquad (3.1f)$$

$$\lim_{y\to\infty}(u_1, v_1, w_1) = (0,0,0), \qquad (3.1g)$$

where $N^2 \equiv \partial^2/\partial y^2 - \alpha^2 - \gamma^2$. In (3.1a–d) the terms proportional to $\mathrm{d}C/\mathrm{d}t$ have been neglected with respect to those proportional to C, because (3.1e) along with the small values assumed by (q_{x1}, q_{z1}) suggests that $\mathrm{d}C/\mathrm{d}t$ is much smaller than C. The main difficulties in solving (3.1) arise because of the terms describing the interaction of flow perturbations with the basic oscillatory flow. However the solution can be found following a procedure similar to that used by Vittori (1992). For sake of brevity we omit the details; the interested reader can find them in Roos (2000). Combining (2.5d) and (3.1e), the amplitude equation for $C(t)$ is obtained:

$$\frac{\mathrm{d}C(t)}{\mathrm{d}t} = g(t)C(t), \qquad (3.2)$$

where two contributions g_1 and g_2, both independent of Ψ, can be identified:

$$g(t) = \frac{-aR_d^{1-b}}{2\Psi^{1/2}(1-n)}2^b\left(g_1(t) - \frac{1}{\Psi}g_2(t)\right), \qquad (3.3)$$

in which

$$g_1(t) = |V_0|^{b-3} \left\{ |V_0|^2 \left[i\alpha \left(u_1 + \frac{\partial u_0}{\partial y} \right) + i\gamma \left(w_1 + \frac{\partial w_0}{\partial y} \right) \right] \right.$$

$$\left. + (b-1)(i\alpha u_0 + i\gamma w_0) \left[u_0 \left(u_1 + \frac{\partial u_0}{\partial y} \right) + w_0 \left(w_1 + \frac{\partial w_0}{\partial y} \right) \right] \right\}, \quad (3.4a)$$

$$g_2(t) = \tfrac{1}{2} \mu R_d |V_0|^{b-3} \{ -|V_0|^2 (\alpha^2 + \gamma^2) + (b-1)(i\alpha u_0 + i\gamma w_0)^2 \}. \quad (3.4b)$$

The former contribution (g_1) is related to the sediment movement induced by the fluid drag while the latter (g_2) is due to the gravity component along the ripple surface. Integration of (3.2) is straightforward and provides

$$C(t) = C_0 \exp \left[\int_0^t g(\tau; \alpha, \gamma, \sigma, R_\delta, R_d, \Psi) d\tau \right]. \quad (3.5)$$

As in Blondeaux (1990) and Vittori & Blondeaux (1992), four contributions to $C(t)$ can be identified. The first two contributions are related to the real and imaginary parts of the time average $\langle g \rangle$ of the function $g(t)$ (herein an angle bracket indicates the time-average value). The real part $\langle g \rangle_r$ controls the amplification of the bottom perturbation while the imaginary part $\langle g \rangle_i$ is related to the migration speed of the bottom waviness. Because of the symmetry of the problem the latter contribution vanishes. The third and fourth contributions are related to the oscillatory part of g with a vanishing time average. These terms describe the small oscillations of the ripple profile around its average position. Thus, for fixed values of the parameters R_δ, R_δ, σ and Ψ, the growth or decay of the bottom perturbations characterized by wavenumbers α and γ, are controlled by a balance between the tendency of sediments to pile up near the crests of the bottom waviness $\langle g_1 \rangle_r$ and their movement in the downslope direction induced by the force of gravity and described by the term $\Psi^{-1} \langle g_2 \rangle_r$. By fixing R_δ, R_d, σ from (3.3), the parameter that determines which effect dominates is the mobility number Ψ. For small Ψ the second term on the right-hand side of (3.3) (g_2/Ψ) dominates the first term (g_1) and the bottom perturbation characterized by wavenumbers α and γ tends to decay. On the other hand, for large Ψ, the first term dominates the second one and the perturbation tends to grow. Moreover, equation (3.3) shows the existence of a marginal value of Ψ for which the two effects exactly balance each other. This marginal value is denoted by Ψ_{marg} and depends on R_δ, R_d, σ as well as the perturbation wavenumbers α and γ:

$$\Psi_{marg}(\alpha, \gamma; \sigma, R_\delta, R_d) = \frac{\langle g_2 \rangle_r}{\langle g_1 \rangle_r}. \quad (3.6)$$

For fixed values of the parameters (R_δ, R_d, σ), equation (3.6) defines a marginal stability surface in the space (α, γ, Ψ). The critical mobility number Ψ_{crit} is defined as the minimum of Ψ_{marg} over the (α, γ)-plane. The critical value of Ψ corresponds to particular values $(\alpha_{crit}, \gamma_{crit})$ of (α, γ). According to the linear theory, when Ψ is smaller than Ψ_{crit}, any perturbation tends to decay and the flat bottom configuration is stable. On the other hand, when Ψ is larger than Ψ_{crit} but close to it, a bottom waviness characterized by a wavenumber close to $(\alpha_{crit}, \gamma_{crit})$ tends to develop.

The results can be conveniently summarized by distinguishing between three cases with respect to σ. See also figure 2, where we note that showing one half of the (α, γ)-plane is sufficient due to the symmetry of the results about the point $(\alpha, \gamma) = (0, 0)$.

(a) For $\sigma = 0$, we find that the marginal conditions are symmetric with respect to the line $\gamma = 0$. In this case the flow at the top of the bottom boundary layer is
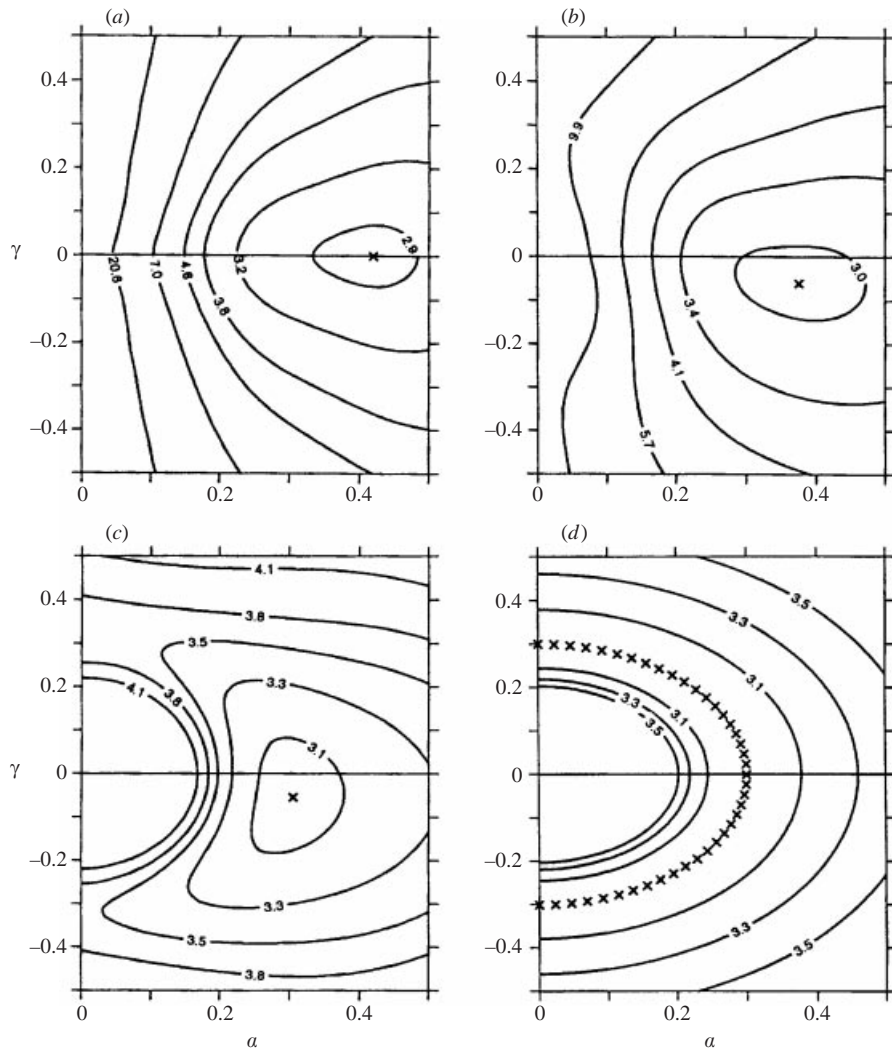
FIGURE 2. Contour plots of the marginal stability surface $\Psi_{marg}(\alpha, \gamma)$ for different values of σ and $R_\delta = 30$, $R_d = 10$. Crosses indicate critical wavenumber(s) $(\alpha_{crit}, \gamma_{crit})$. (a) $\sigma = 0$, symmetric with respect to the line $\gamma = 0$; (b) $\sigma = 0.5$ and (c) $\sigma = 0.9$, where the symmetry is lost and Ψ_{crit} is found off the line $\gamma = 0$; (d) $\sigma = 1$, obeying rotational symmetry, where the critical wavenumbers form a semicircle.

unidirectional oscillatory, making the perturbation characterized by α and γ and that characterized by α and $-\gamma$ physically identical. Moreover, we find that $\Psi_{marg}(\alpha, 0) < \Psi_{marg}(\alpha, \gamma)$ for non-zero γ. This means that the most unstable perturbations are two-dimensional. In particular Ψ_{crit} always lies on the line $\gamma = 0$. We note that this finding is in contradiction with the results described in Vittori & Blondeaux (1992). However, in developing the computer program for the evaluation of Ψ_{marg}, it was found that the code by Vittori & Blondeaux (1992) contains an error, giving rise to some erroneous conclusions. However, the final results described by Vittori & Blondeaux (1992), i.e. the regions in the parameter space where brick-pattern ripples are expected to form, are only affected by a small quantitative error and the mechanism leading to the formation of brick-pattern ripples does not change, i.e. three-dimensional bedforms

appear because of a resonant interaction among different components of the bottom perturbation.

(*b*) For $\sigma > 0$ (but $\sigma \neq 1$), i.e. in the case of an elliptical (but not circular) upper flow, the above finding no longer holds. The results show that the symmetry with respect to the line $\gamma = 0$ is lost. This is due to the boundary condition at the top of the viscous boundary layer. This condition is characterized by an orientation that reverses with respect to the bottom perturbation when γ is replaced with $-\gamma$. Moreover, in this case, Ψ_{crit} is found off the line $\gamma = 0$, i.e. $\gamma_{crit} \neq 0$. This means that the crests of the most unstable mode and the major axis of the elliptical flow outside the bottom boundary layer are no longer perpendicular. However, the angle of deviation is found to be small even for values of σ close to one.

(*c*) The case $\sigma = 1$ corresponds to a circular upper flow. In this situation the boundary conditions obey rotational symmetry about the origin of the (α, γ)-plane. This property reflects the trivial observation that, for a given bottom perturbation, the orientation of the *x*- and *z*-axes should not affect the boundary conditions.

A linear stability analysis shows which perturbation component in the form (2.3) is most likely to develop. However it cannot explain the three-dimensional bottom forms observed during some laboratory and field experiments which indicate that the oscillatory flow (2.2) can lead to the appearance of brick-pattern ripples, tile ripples or other three-dimensional bottom configurations different from (2.3). As suggested by Vittori & Blondeaux (1992), to explain three-dimensional bottom configurations, it is necessary to take into account nonlinear effects. Inspired by an idea by Craik (1971), Vittori & Blondeaux (1992) showed that the nonlinear interaction of two-dimensional and three-dimensional bottom perturbations driven by a unidirectional oscillatory flow is the mechanism by which brick-pattern ripples appear. In the following section we follow Vittori & Blondeaux (1992) and show that brick-pattern ripples and tile ripples are triggered by the same mechanism, the former being induced by a unidirectional oscillatory flow while tile ripples are associated with a flow described by (2.1) with σ close to one. Hence it is possible to conclude that different three-dimensional bedforms are associated with different values of σ, $\sigma = 0$ (unidirectional oscillatory flow) and $\sigma = 1$ (circular flow) being the two extreme cases.

4. Nonlinear interaction of three components of the bottom perturbation: formation of three-dimensional bottom patterns

Let us consider a set of three perturbation components, each characterized by a wave vector (α_j, γ_j) $(j = 1, 2, 3)$ and hence proportional to $E_j = \mathrm{e}^{\mathrm{i}(\alpha_j x + \gamma_j z)}$ and its complex conjugate $\bar{E}_j = \mathrm{e}^{-\mathrm{i}(\alpha_j x + \gamma_j z)}$. As discussed by Craik (1971) the interaction of these perturbation components is particularly strong when adding two of the wave vectors gives the third one:

$$(\alpha_1, \gamma_1) = (\alpha_2, \gamma_2) + (\alpha_3, \gamma_3). \tag{4.1}$$

This can be understood by realizing that the model equations at order ϵ^2 contain products of first-order components. Condition (4.1) implies $E_1 = E_2 E_3$, so products of mode 2 and 3 components contribute to mode 1. Also the other combinations imply energy transfer within the system: $E_2 = E_1 \bar{E}_3$ and $E_3 = E_1 \bar{E}_2$. This energy transfer could lead to an explosive growth of the triad resulting in three-dimensional ripple patterns. Here, explosive growth means an asymptotic growth faster than the exponential growth predicted by the linear theory. Hence, the amplitudes of the three perturbations tend to reach an infinite value in a finite time. An example of this explosive growth is plotted in figure 5(*a*) below.

As discussed in Vittori & Blondeaux (1992), a necessary condition for the mechanism sketched above to be physically relevant is that the actual mobility number Ψ is close to each of the marginal mobility numbers $\Psi_{marg,j} \equiv \Psi_{marg}(\alpha_j, \gamma_j)$ of the three perturbations:

$$\Psi = \Psi_{marg,j}(1 + \epsilon\kappa_j) \quad (j = 1, 2, 3), \tag{4.2}$$

with ϵ a small parameter and κ_j of order one. We note the ϵ in the linear theory (see (2.3) and (2.4)) as well as in the weakly nonlinear analysis (see (4.4) below) is related to the amplitude of the bottom perturbation. However in the former case ϵ can assume any value as long as $\epsilon \ll 1$, while in the nonlinear context, the value of ϵ depends on the actual mobility number Ψ and on the three marginal mobility numbers $\Psi_{marg,j}$. Assumption (4.2) requires that Ψ is simultaneously close to each of the marginal mobility numbers $\Psi_{marg,1}$, $\Psi_{marg,2}$, $\Psi_{marg,3}$. Thus, it appears that assumption (4.2) can be fulfilled only if the three marginal mobility numbers are close to one another. Hence, to apply the theory it is necessary for the quantity Ω, defined by

$$\Omega \equiv \frac{\max\{\Psi_{marg,2}, \Psi_{marg,3}\} - \Psi_{marg,1}}{\Psi_{marg,1}}, \tag{4.3}$$

to be smaller than one.

Assuming that (4.2) is satisfied, let us consider the following structure of the bottom perturbation:

$$\eta(x, z, t) = \epsilon \left[\sum_{j=1}^{3} A_j(\tau) C_j(t) e^{i(\alpha_j x + \gamma_j z)} + \text{c.c.} \right]$$

$$+ \epsilon^2 \left[\sum_{j=1}^{3} B_j(\tau) D_j(t) e^{i(\alpha_j x + \gamma_j z)} + \text{c.c.} \right.$$

$$\left. + \text{terms proportional to } e^{\pm 2i(\alpha_j x + \gamma_j z)} \right] + O(\epsilon^3), \tag{4.4}$$

where, as suggested by Vittori & Blondeaux (1992), the amplitudes of the three perturbation components are assumed to depend on the slow time variable τ defined by

$$\tau = \epsilon Q t, \quad Q = \frac{a R_d^{1-b}}{(1-n)2\Psi^{1/2}}. \tag{4.5}$$

For typical values of R_d and Ψ for sand underneath surface gravity waves, Q turns out to be of order 10^{-3}, thus showing that the morphodynamic and the hydrodynamic time scales are far apart.

Because of the presence of the bottom waviness, perturbations of the basic flow (2.2) characterizing the flat bottom case are induced. Since $\epsilon \ll 1$, it is appropriate to expect the flow field to be in the form

$$\boldsymbol{v} = (u_0(y,t), 0, w_0(y,t)) + \epsilon \left[\sum_{j=1}^{3} A_j(\tau) C_j(t) \boldsymbol{v}_{1j}(y,t) e^{i(\alpha_j x + \gamma_j z)} + \text{c.c.} \right]$$

$$+ \epsilon^2 \left[\sum_{j=1}^{3} B_j(\tau) D_j(t) \boldsymbol{v}_{2j}(y,t) e^{i(\alpha_j x + \gamma_j z)} + \text{c.c.} \right.$$

$$\left. + \text{terms proportional to } e^{\pm 2i(\alpha_j x + \gamma_j z)} \right] + O(\epsilon^3). \tag{4.6}$$

Similar expressions hold for the pressure field and the sediment transport rate. Substitution of (4.6) into (2.5a–d) and collecting terms of the same order of magnitude gives rise to different problems. At order ϵ^0 the solution is provided by (2.10). At order ϵ the solution can be found by following the procedure briefly outlined in the previous section. Because of assumption (4.2), the amplitudes of the perturbation components neither increase nor decay at this order of approximation. Hence the functions $C_j(t)$ ($j = 1, 2, 3$) are given by the sum of a constant which, without loss of generality, can be assumed equal to one, and periodic functions with a vanishing time average. The functions $A_j(\tau)$ ($j = 1, 2, 3$) are left unknown.

We omit details of the problem found at order ϵ^2. The sediment continuity equation provides three ordinary differential equations involving the unknowns $A_j(\tau)$ and $D_j(t)$ (see (4.4)). The functions $D_j(t)$, which describe the oscillations, during the wave cycle, of the perturbation components of order ϵ^2, should be periodic functions of t and the time average of $\mathrm{d}D_j/\mathrm{d}t$ should vanish. Therefore, taking the time average of the sediment continuity equation and forcing the vanishing of $\langle \mathrm{d}D_j/\mathrm{d}t \rangle$, a set of ordinary differential equations for A_j is obtained, the coefficients of which depend on the solution of the hydrodynamic part of the problem. However, as explained in Vittori & Blondeaux (1992), in order to determine the time development of $A_j(\tau)$, it is not necessary to solve the problem for v_{2j}. Indeed by assuming that d^* is much smaller than δ^*, some algebraic manipulations of the sediment continuity equation lead to the following system of three ordinary differential equations for the amplitude functions $A_j(\tau)$ ($j = 1, 2, 3$):

$$\frac{\mathrm{d}A_1}{\mathrm{d}\tau} = \langle a_1 \rangle A_1 + \langle b_1 \rangle A_2 A_3, \tag{4.7a}$$

$$\frac{\mathrm{d}A_2}{\mathrm{d}\tau} = \langle a_2 \rangle A_2 + \langle b_2 \rangle A_1 \bar{A}_3, \tag{4.7b}$$

$$\frac{\mathrm{d}A_3}{\mathrm{d}\tau} = \langle a_3 \rangle A_3 + \langle b_3 \rangle A_1 \bar{A}_2, \tag{4.7c}$$

where the coefficients a_j, b_j ($j = 1, 2, 3$) are given in the Appendix and do not depend on v_{2j}. The system (4.7) is equivalent to that found by Vittori & Blondeaux (1992), but the coefficients are different because of the presence of a transverse velocity w_0 and the flow generated by its interaction with the bottom waviness. Only for $\sigma = 0$, implying $w_0 = 0$, do the expressions providing a_j and b_j ($j = 1, 2, 3$) simplify considerably and the original results by Vittori & Blondeaux (1992) are recovered.

The right-hand side of each equation in (4.7) contains two terms. When the amplitudes A_j of the bottom perturbation components are small, the first term, which is linear and due to the interaction of the perturbation with the basic flow, induces an exponential growth or decay of the generic components, depending on the sign of a_j (which equals the sign of $\Psi - \Psi_{marg,j}$). This implies $\langle a_j \rangle < 0$ in subcritical conditions ($\Psi < \Psi_{marg,j}$) and $\langle a_j \rangle > 0$ in supercritical conditions ($\Psi > \Psi_{marg,j}$). In this way the fundamental results of the linear theory are retained. The growth or decay takes place on the slow time scale τ (see (4.5)), because the assumption (4.2) implies small amplification rates. The second term is related to the nonlinear interaction among the different components and modifies the behaviour of A_j predicted by the linear analysis depending on the relative signs of $\langle a_j \rangle$, $\langle b_j \rangle$. We note that the value of $\langle a_j \rangle$ depends on the parameters (σ, R_δ, R_d, Ψ), whereas $\langle b_j \rangle$ is independent of the mobility number and depends only on (σ, R_δ, R_d).

Before discussing the results, let us look at the possible bottom configurations generated by (4.4). Vittori & Blondeaux (1992) considered the superposition of three perturbations with wave numbers

$$(\alpha_{crit}, 0), \quad (\tfrac{1}{2}\alpha_{crit}, \gamma), \quad (\tfrac{1}{2}\alpha_{crit}, -\gamma), \tag{4.8}$$

where the value of α_{crit} comes from the linear theory when $\sigma = 0$ and γ is treated as a parameter. Figure 3(b) shows a plot of the predicted bottom configuration, clearly featuring a typical brick-pattern ripple configuration. The first component will be called the main component, whereas the second and third components will be called oblique components. The bridges connecting the main ripple crests are formed by the two oblique components. Vittori & Blondeaux (1992) found that the growth of the amplitude of the oblique components is usually slower than that of the main component. This result justifies the choice of an amplitude of the bridges lower than that of the main crests. In the range of the parameters investigated by Vittori & Blondeaux (1992), the values of γ giving rise to the most rapid growth of the three-dimensional bottom configuration are smaller than α_{crit}. Therefore the spanwise wavelength of the bedforms is larger than the longitudinal wavelength.

The same set of bottom perturbations (4.4) and (4.8) can be used to construct a sketch of a bottom configuration which resembles hexagonal ripples (see figure 3c). Obviously a hexagonal ripple pattern requires different characteristics of the perturbation components. First it is essential that the three amplitudes develop according to $A_1 \equiv A_2 \equiv -A_3$, i.e. with more or less equal magnitudes and with correct signs. Then, to obtain purely hexagonal patterns (i.e. not stretched in one direction), it is necessary that $\gamma = \tfrac{1}{2}\sqrt{3}\alpha_{crit}$. Thus it remains to show that forcing conditions exist such that the values of γ giving rise to the quickest growth of the bottom perturbations are close to $\tfrac{1}{2}\sqrt{3}\alpha_{crit}$ and that the amplitudes A_j grow at the same rate. In this case tile ripples would be the bedform predicted by the theory. Further bottom configurations can be obtained for different choices of the parameters. For example with the same wavenumbers as in 3(c), but with $A_1 = A_2 = A_3$, the bottom configuration, which is sketched in figure 3(d), appears to be characterized by regular bumps, i.e. upside-down hexagonal ripples. At this stage it is worth pointing out that complex three-dimensional bottom configurations, which cannot be traced back to brick-pattern or tile ripples, have been observed during experiments performed by K. H. Andersen (2000, private communication). Of course the choice $\gamma_1 = 0$ and $\gamma_2 = -\gamma_3$ generates bottom configurations which are symmetric with respect to the x-axis. More complex bottom forms are generated for arbitrary values of (α_1, γ_1), (α_2, γ_2), (α_3, γ_3). An example is provided in figure 3(e) where $\gamma_1 = 0$, $\alpha_2 = 0.8\alpha_1$ and $\gamma_2 = 0.2\alpha_1$. Finally when $A_2 \equiv A_3 \equiv 0$, two-dimensional ripples are found (see figure 3a). Vittori & Blondeaux (1992) showed that for a unidirectional oscillatory flow both two-dimensional ripples and brick-pattern ripples can be generated. In the following it is shown that a circular flow can generate tile ripples, while distorted brick-pattern ripples or distorted tile ripples are generated by elliptical flows. The former tend to appear when σ is close to zero, while the latter form when σ tends to one.

5. Discussion of the results: general remarks

As previously pointed out, Vittori & Blondeaux (1992) restricted themselves to triads of the form (4.8), i.e. they considered wavenumber vectors which are symmetric with respect to the α-axis. This symmetry is desirable in the case of brick-pattern ripples and it is appropriate when considering unidirectional oscillatory flows which
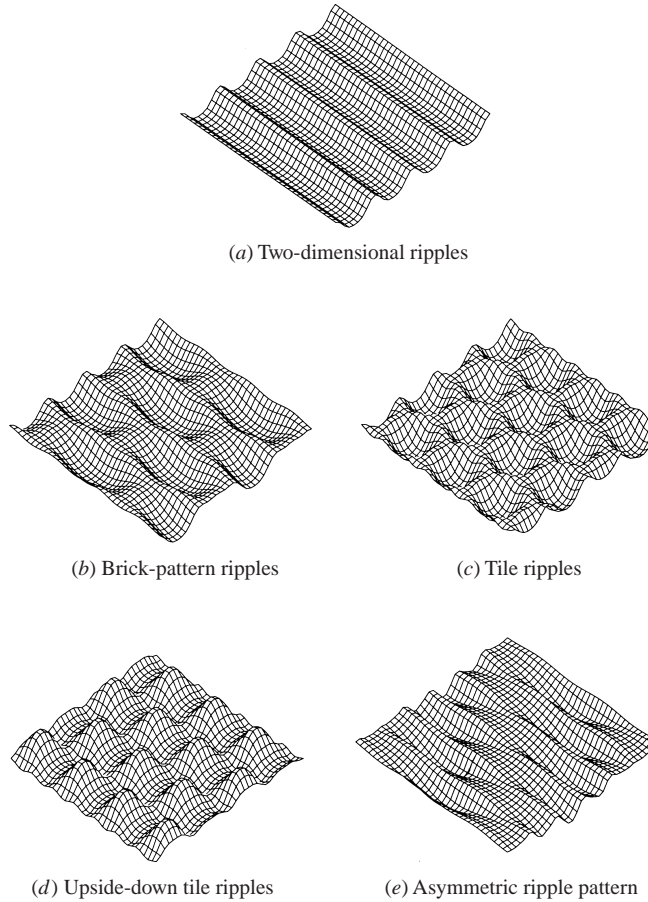
(*a*) Two-dimensional ripples

(*b*) Brick-pattern ripples

(*c*) Tile ripples

(*d*) Upside-down tile ripples

(*e*) Asymmetric ripple pattern

FIGURE 3. Sketch of various bottom configurations, representing ripple patterns studied with the present model and (4.8). (*a*) Two-dimensional ripples are represented by a single bottom perturbation ($A_1 \neq 0$, $A_2 \equiv A_3 \equiv 0$). (*b*) Brick-pattern ripples are generated by $A_2 = -A_3$, $A_1 > A_2$ and $\gamma < \alpha_{crit}$. (*c*) Hexagonal ripples or tile ripples are generated by $A_1 = A_2 = -A_3$ and $\gamma = \frac{1}{2}\sqrt{3}\alpha_{crit}$. (*d*) Upside-down hexagonal ripples for $A_1 = A_2 = A_3$. (*e*) Example of a three-dimensional ripple pattern asymmetric with respect to the *x*-axis (*x*-axis from bottom left to top right).

are directed along the *x*-axis. However, for forcing flows described by (2.1), any triad might be relevant, as long as condition (4.1) is satisfied. In this section we generalize the results of Vittori & Blondeaux (1992) allowing for triads of a more general form. However to simplify the discussion of the results, we choose the main component according to the linear analysis: $(\alpha_1, \gamma_1) = (\alpha_{crit}, \gamma_{crit})$. In this way we investigate how the (linearly) most unstable perturbation component interacts with other components. Hence, the triad is given by

$$(\alpha_{crit}, \gamma_{crit}), \quad (\alpha_2, \gamma_2), \quad (\alpha_3, \gamma_3) = (\alpha_{crit} - \alpha_2, \gamma_{crit} - \gamma_2), \tag{5.1}$$

where (α_2, γ_2) can be chosen freely. One criterion which can be used to single out the values of α_2, γ_2 which are more likely to be observed in the field is that of choosing the values which give rise to the strongest coupling between the different components of the bottom perturbation and to the quickest growth of the bottom configuration. Therefore, for a given set of the parameters $\{\sigma, R_\delta, R_d\}$ we compute the coefficients
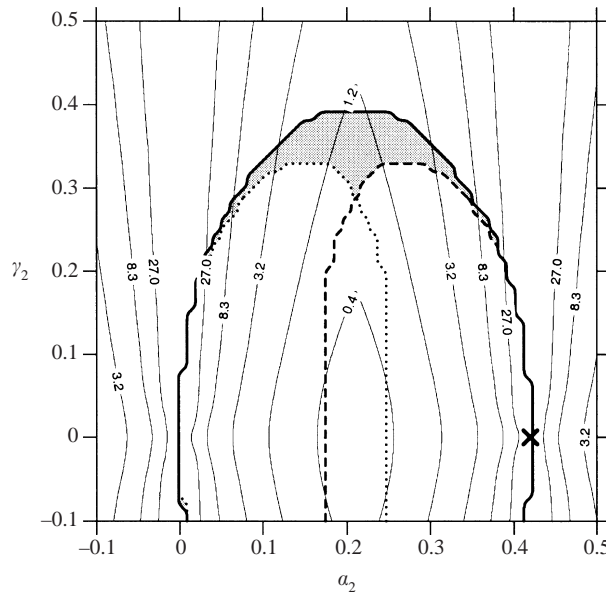
FIGURE 4. Plot of $\langle b_j \rangle = 0$ lines in the (α_2, γ_2)-plane for $\sigma = 0$, $R_\delta = 30$ and $R_d = 10$. Solid isoline: $\langle b_1 \rangle = 0$, dashed isoline: $\langle b_2 \rangle = 0$, dotted isoline: $\langle b_3 \rangle = 0$. In the grey area all $\langle b_j \rangle$ are negative. Also plotted are contour curves of Ω. The critical wavenumber $(\alpha_{crit}, \gamma_{crit}) = (0.42, 0)$ (with $\Psi_{crit} = 2.87$) is denoted with a cross.

$\langle a_j \rangle$, $\langle b_j \rangle$ as a function of (α_2, γ_2) and perform the numerical integration of (4.7). Of course the solution depends also on the initial conditions. For convenience, we assume $A_1 = A_2 = 1$ and $A_3 = -1$ at $\tau = 0$. To observe the growth of bottom patterns, starting from small perturbations, at least one of the $\langle a_j \rangle$ should be positive. Hence, in the following we will consider cases for which $\Psi > \Psi_{crit}$, as this implies that $\langle a_1 \rangle > 0$. Even though (α_2, γ_2) can be chosen freely, we remind the reader that assumption (4.2) should always be satisfied, i.e. $\Psi_{marg,2}$ and $\Psi_{marg,3}$ should be close to the value of Ψ. For values of the parameters of physical relevance, $\Psi_{marg,2}$ and $\Psi_{marg,3}$ are significantly larger than Ψ_{crit} when (α_2, γ_2) and (α_3, γ_3) move away from (α_1, γ_1). Hence, unless (α_2, γ_2) and (α_3, α_3) are close to (α_1, γ_1) it turns out that $\Psi_{crit} < \Psi < \min\{\Psi_{marg,2}, \Psi_{marg,3}\}$ and both $\langle a_2 \rangle$ and $\langle a_3 \rangle$ are negative. In this case, according to the linear theory, A_1 should amplify while A_2 and A_3 should decay.

In the present case, we will show that nonlinear effects modify these conclusions. Numerical experiments indicate that the qualitative behaviour of A_j depends in particular on the combination of the signs of $\langle b_j \rangle$. Therefore we discuss the results fixing the parameters of the problem and looking at the sign of $\langle b_j \rangle$ in the plane (α_2, γ_2). When $\sigma = 0$, $R_\delta = 30$ and $R_d = 10$, the curves in the (α_2, γ_2)-plane, for which the values of $\langle b_j \rangle$ vanish, are plotted in figure 4. Above the solid line, the values of $\langle b_1 \rangle$ are positive while $\langle b_1 \rangle$ is negative below it. On the other hand above the dashed line and the dotted line the values of $\langle b_2 \rangle$ and $\langle b_3 \rangle$, respectively, are negative while $\langle b_2 \rangle$ and $\langle b_3 \rangle$ are positive below. Numerical experiments show that an explosive growth of the three perturbation components takes place only if all the coefficients $\langle b_j \rangle$ are negative. Therefore three-dimensional ripples are expected to appear in the grey area (resonance area) of figure 4. Note that an interaction between the different components of the bottom perturbation (4.4) is also present when $\langle b_1 \rangle$ has the opposite sign to both $\langle b_2 \rangle$ and $\langle b_3 \rangle$. However such an interaction leads to a much
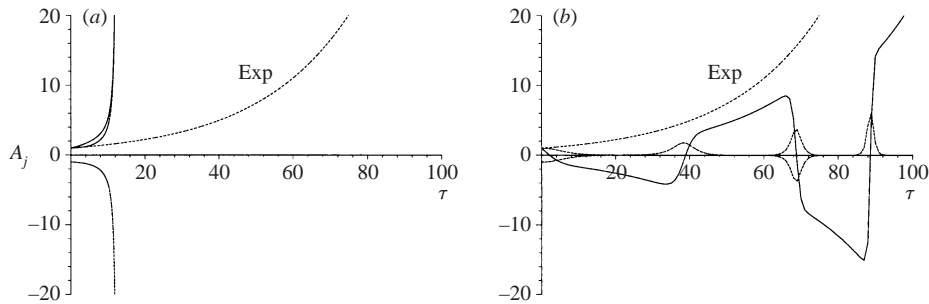
FIGURE 5. Example of amplitude development (*a*) explosive growth, i.e. faster than exponential growth, giving rise to three-dimensional patterns, is observed when all $\langle b_j \rangle$ are negative; (*b*) growth slower than exponential, hence no resonance, observed when $\langle b_1 \rangle$ has the opposite sign to both $\langle b_2 \rangle$ and $\langle b_3 \rangle$. Plotted are A_1 (solid line), A_2 and A_3 (dashed line) and the plain exponential growth obtained when nonlinear effects are neglected. Parameters: $\langle a_1 \rangle = 0.04$, $\langle a_2 \rangle = \langle a_3 \rangle = -0.08$, $\langle b_2 \rangle = \langle b_3 \rangle = -0.01$ and for case (*a*) $\langle b_1 \rangle = -0.01$, while for case (*b*) $\langle b_1 \rangle = 0.5$.

weaker and slower growth of the perturbation components (see examples of the time development of A_j in figure 5). All points within the grey area of figure 4 correspond to a resonant triad, at first sight leaving us with a large amount of possibilities for formation of three-dimensional bed configurations. However, as previously pointed out, assumption (4.2) implies that the value of Ω defined by (4.3) should be small. Hence, for fixed values of the parameters, triads which lead to large values of Ω should not be taken into account. For this reason in figure 4 contour lines of Ω are also plotted. Assuming that the most preferred triad is that corresponding to the smallest value of Ω, figure 4 shows that the expected values of α_2 and γ_2 are about 0.21 and 0.28, respectively. This exactly justifies the choice by Vittori & Blondeaux (1992) to restrict to triads of the form (4.8). The reason for expecting the appearance of brick-pattern ripples instead of two-dimensional ripples lies in the fact that the growth of the three-dimensional bottom configuration is explosive when (α_2, γ_2) falls in the grey area of figure 4 while the growth of the two-dimensional component is only exponential or slower outside it. Because of the values of $\langle a_j \rangle$ previously discussed, $|A_1|$ becomes larger than $|A_2|$ and $|A_3|$. Moreover the value of $\gamma_3 = -\gamma_2$ inducing the fastest growth of the bottom perturbation is smaller than α_{crit} and the overall bottom configuration is similar to that of brick-pattern ripples, as sketched in figure 3(*b*).

Different values of the parameters imply quantitative differences in the results we have just discussed. In particular the extent of the grey area tends to decrease when R_δ is decreased, keeping the other parameters fixed, and disappears for R_δ smaller than a critical value. Hence, three-dimensional ripples do not appear when R_δ is below this critical value. A comparison between theoretical findings and experimental data concerning brick-pattern ripples only, is described in Vittori & Blondeaux (1992). The agreement between the predicted longitudinal and transverse wavelengths and the observed ones (Sleath & Ellis 1978) is fair. Also the regions of existence of brick-pattern ripples in the parameter space are predicted rather well. Because of the assumption of a laminar flow, Vittori & Blondeaux (1992) considered only the data by Sleath & Ellis (1978) characterized by moderate values of R_δ.

6. Discussion of the results: effect of ellipticity

On increasing σ the curves in figure 4 and the resonance area are modified. Also the distribution of Ω changes. Figure 6 shows the gradual deformation of the $\langle b_j \rangle = 0$

Figure	σ	$\alpha_{crit}(=\alpha_1)$	$\gamma_{crit}(=\gamma_1)$	$\Psi_{crit}(=\Psi_{marg,1})$
6(*a*)	0	0.42	0	2.87
6(*b*)	0.25	0.41	−0.03	2.88
6(*c*)	0.5	0.38	−0.06	2.91
6(*d*)	0.75	0.32	−0.06	2.95
6(*e*)	0.9	0.30	−0.05	2.98
6(*f*)	1	0.30	0	3.01

TABLE 1. Critical conditions, i.e. results of the linear theory, for the cases presented in figure 6 ($R_\delta = 30$, $R_d = 10$). Note that for $\sigma = 1$, due to the rotational symmetry discussed in §3, every wave vector (α, γ) with magnitude 0.30 is critical. Without loss of generality we choose the one with $\gamma_{crit} = 0$.

curves and the resonance area for different values of σ. As discussed previously, three-dimensional bedforms tend to appear when the values of (α_2, γ_2) fall in the grey area. It is worth remembering that the results of the linear analysis now imply $\gamma_1 \neq 0$, i.e. the critical wavenumber falls off the α-axis. Hence the bottom configuration is no longer symmetric with respect to the x-axis (see also table 1). These results make the orientation of three-dimensional bottom configurations slightly different from that of the x-axis, although the deviation is very small. For small values of σ (figure 6*b*) no qualitative change is induced. For increasing σ (figure 6*c*), new curves appear giving rise to resonance areas for near zero values of α_2. However these areas are characterized by large values of Ω and the corresponding triads are not expected to amplify. Increasing the ellipticity further, we see that the new resonance areas approach the first one (figure 6*d*) and become close to it (figure 6*e*). The final plot (figure 6*f*) should be interpreted as the result of this complex behaviour of the $\langle b_j \rangle = 0$ curves when σ equals 1. As already pointed out in discussing the results of the linear analysis, when $\sigma = 1$ the orientation of the x- and z-axes does not affect the results, because the flow outside the bottom boundary layer (i.e. the forcing term of the problem) obeys rotational symmetry about the origin. The results shown in figure 6(*f*) have been obtained fixing $(\alpha_1, \gamma_1) = (\alpha_{crit}, 0)$, i.e. choosing the x-axis normal to the crests of the first mode. However, any other choice would lead to the same results.

The appearance of new and large resonance areas, when σ is increased, multiplies the number of resonant triads and makes it more difficult to identify the morphological patterns that would tend to appear. A criterion which can be used to single out the most unstable triad is that previously discussed, i.e. the three values of (α_j, γ_j) can be chosen such that the associated value of Ω is minimal, which indicates that (4.2) can be satisfied. Hence looking at figure 6(*f*), it appears that the values of (α_2, γ_2) which are most likely to develop are $(0.15, 0.26)$. Since $(\alpha_1, \gamma_1) = (0.30, 0)$ (see table 1) this implies $(\alpha_3, \gamma_3) = (0.15, -0.26)$ and these values show that a circular flow tends to form tile ripples. For values of σ different from 1 but close to it, ripples similar to tile ripples are the bedforms predicted by the theory, although the bottom configuration is slightly distorted with respect to that shown in figure 3(*c*).

Changing the values of the parameters affects the extent of the resonance area. In particular the extent of the resonance area tends to decrease when R_δ is decreased keeping the other parameters fixed. Figure 7 shows an example in which decreasing R_δ makes the resonance area disappear. The results of figure 7 along with those of figure 6(*c*) show that for $\sigma = 0.5$ and $R_\delta = 10$, three-dimensional ripples do not appear
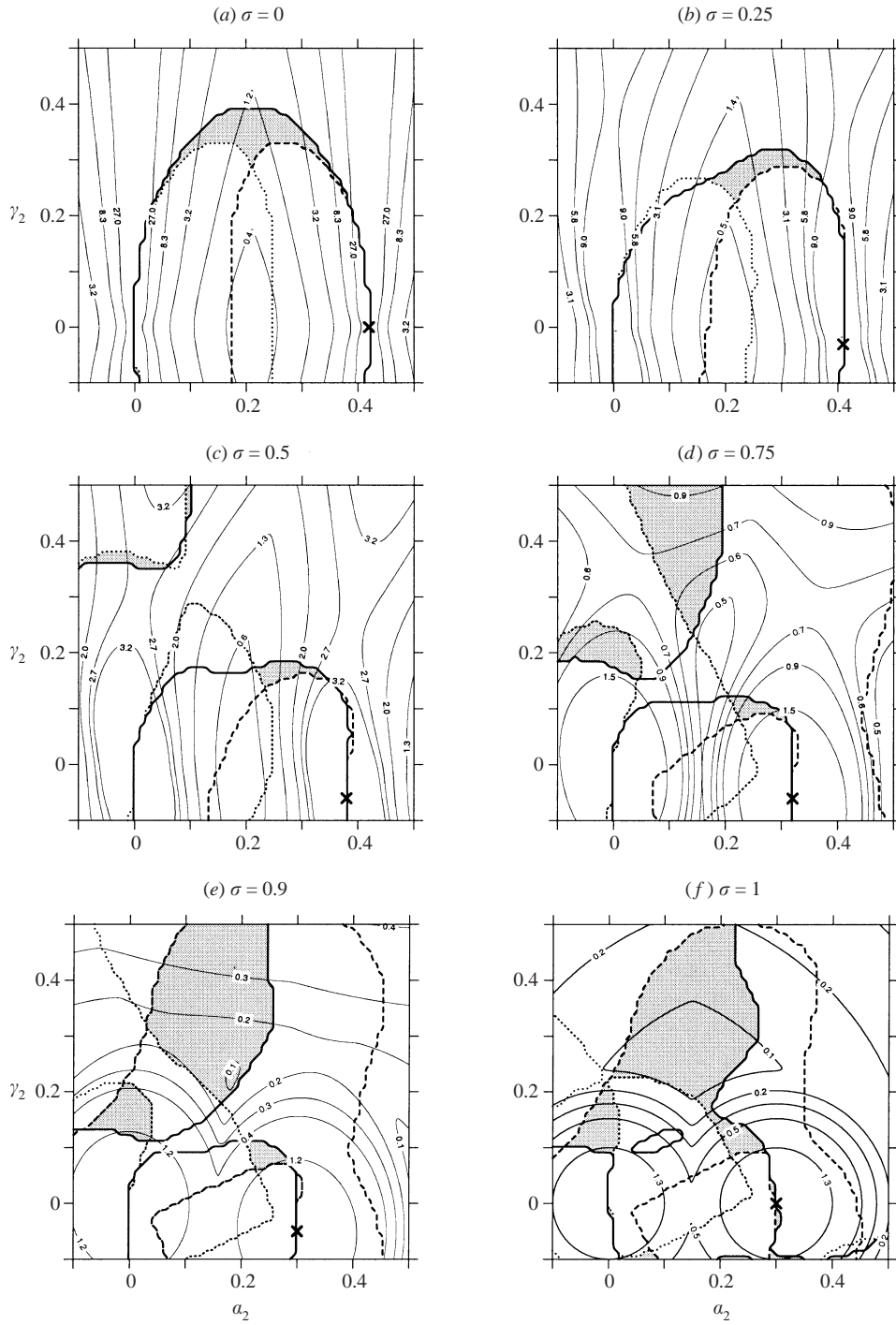
FIGURE 6. Plot of $\langle b_j \rangle = 0$ lines and the resonance area (grey) in the (α_2, γ_2)-plane for different values of σ and for $R_\delta = 30$, $R_d = 10$. See caption of figure 4 for explanation and table 1 for an overview of the critical conditions.
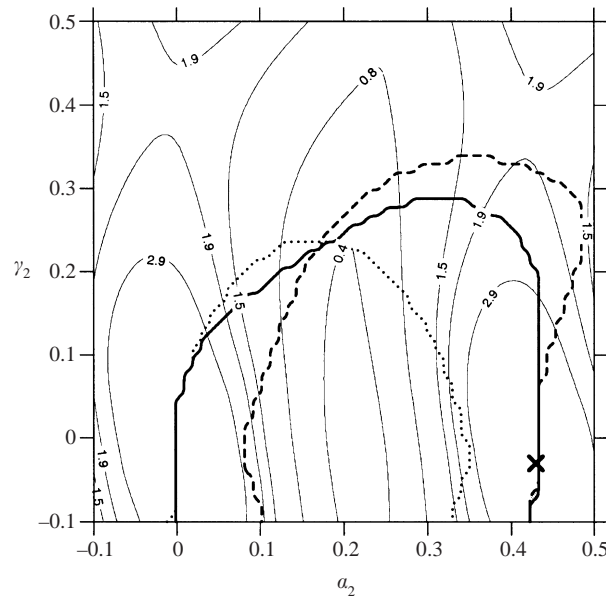
FIGURE 7. Example of disappearing resonance area for $\sigma = 0.5$, $R_\delta = 15$ and $R_d = 10$, giving $(\alpha_{crit}, \gamma_{crit}) = (0.43, -0.03)$ with $\Psi_{crit} = 2.56$. Compare with figure 6(*c*). See caption of figure 4 for explanation.

when R_δ is smaller than about 15, whatever value is taken by the mobility number characterizing the sediment. Of course when Ψ is larger than Ψ_{crit}, two-dimensional ripples appear. On the other hand, for R_δ larger than 15, inequant hexagonal tile ripples tend to develop, provided the actual value of the mobility number exceeds Ψ_{crit}. The theory also permits evaluating the longitudinal and transverse wavelengths of the bottom configuration. For example, as shown in figure 6(*c*), for $R_\delta = 30$ the longitudinal wavelength turns out to be about $16\delta^*$ while the transverse wavelength is about $40\delta^*$. Similar results can be obtained for different values of σ and R_δ. We note that for values of σ close to unity, the resonance area is rather large and it is still present even for small values of R_δ. Hence, when the flow outside the bottom boundary layer is characterized by circular trajectories in a horizontal plane, equant hexagonal ripples tend to form whatever value of R_δ is considered, provided the mobility number is larger than Ψ_{crit}, and two-dimensional ripples cannot be observed. This qualitative theoretical finding is supported by the experimental observations by Jan & Lin (1998). Unfortunately, quantitative measurements of bedforms and flow characteristics for experimental conditions characterized by values of σ close to unity are not available or have been obtained when the flow regime in the bottom boundary layer is turbulent (Jan & Lin 1998). Hence a quantitative comparison between theoretical findings and experimental observations cannot be made.

7. Conclusions

The mechanism giving rise to three-dimensional bedforms under sea waves has been investigated. The wave field originates from an incoming wave approaching the coast at an arbitrary angle and being partially reflected. Hence sediment motion and ripple appearance are driven by a flow field which, just outside the bottom boundary layer, harmonically oscillates in two orthogonal horizontal directions with the same angular frequency but with different amplitudes and a phase shift of $\pi/2$. The work is based

on a weakly nonlinear stability analysis of the flat bottom configuration and extends the research carried out by Blondeaux (1990), Vittori & Blondeaux (1990, 1992) and Blondeaux *et al.* (2000). In particular, the mechanism of energy transfer within a resonant triad of bottom perturbations, first analysed by Vittori & Blondeaux (1992) to explain the formation of brick-pattern ripples by an oscillatory unidirectional flow, is investigated in the case of a horizontal elliptical flow of eccentricity σ. The main conclusion of the present work is that, for the more general forcing conditions, the same mechanism can account for the formation of other three-dimensional ripple patterns. The characteristics of the bedforms that are likely to appear depend strongly on the ellipticity σ. In particular, tile ripples are associated with a near circular flow (σ close to one), while brick-pattern ripples are related to a unidirectional oscillatory flow (σ close to zero). Thus, the present theoretical work agrees with an experimental observation by Jan & Lin (1998): circular flow outside the bottom boundary layer coincides with the presence of tile ripples.

In formulating the problem and looking for its solution assumptions have been introduced. It is important to realize that a viscous flow is assumed, whence the analysis is restricted to moderate values of the flow Reynolds number (Vittori & Blondeaux 1990 suggest $R_\delta < 100$). Moreover, the assumption of a smooth wavy bed requires the grain size d^* to be much smaller than the thickness of the bottom boundary layer δ^*. Notwithstanding these restrictions, the theory allows the prediction of ripple appearance for flow and sediment characteristics that are easy to reproduce in laboratory experiments as discussed in Blondeaux (1990), Vittori & Blondeaux (1990, 1992) and Blondeaux *et al.* (2000). Moreover, perturbations of small amplitude are considered. Therefore the theoretical results described in the paper strictly deal with the early stages of ripple development. When the ripple amplitude attains large values, the viscous bottom boundary layer separates from the ripple crests and generates large vortex structures characterized by highly nonlinear dynamics. These strong nonlinear effects cannot be handled by the weakly nonlinear analysis developed in the present work and the characteristics of ripples at equilibrium may be different from the theoretical predictions as demonstrated by Stegner & Wesfreid (1999). However, previous weakly nonlinear stability analyses of morphological patterns of both coastal (Vittori & Blondeaux 1990, 1992; Vittori, de Swart & Blondeaux 1999) and fluvial environments (Colombini, Seminara & Tubino 1987; Schielen, Doelman & de Swart 1993) have shown that the analyses certainly help in understanding the mechanisms leading to the appearance of particular bottom configurations and sometimes provide reliable predictions of some bedform characteristics even far from the critical conditions when nonlinear effects are strong and the analyses are not strictly valid.

Appendix

The expressions for a_j, b_j $(j = 1, 2, 3)$ appearing in (4.7) are

$$a_j = 2|2V_0|^{b-3} M_j \kappa_j \left\{ |2V_0|^2 (\alpha_j^2 + \gamma_j^2) + (b-1)(2\alpha_j u_0 + 2\gamma_j w_0)^2 \right\}, \qquad (A\,1)$$

$$b_1 = (b-1)|2V_0|^{b-3}\left\{\left[2u_0\left(2u_{12}+2\frac{\partial u_0}{\partial y}-M_1\mathrm{i}\alpha_2\right)+2w_0\left(2w_{12}+2\frac{\partial w_0}{\partial y}-M_1\mathrm{i}\gamma_2\right)\right]\right.$$

$$\times\left[\mathrm{i}\alpha_1\left(2u_{13}+2\frac{\partial u_0}{\partial y}-M_1\mathrm{i}\alpha_3\right)+\mathrm{i}\gamma_1\left(2w_{13}+2\frac{\partial w_0}{\partial y}-M_1\mathrm{i}\gamma_3\right)\right]$$

$$+\left[2u_0\left(2u_{13}+2\frac{\partial u_0}{\partial y}-M_1\mathrm{i}\alpha_3\right)+2w_0\left(2w_{13}+2\frac{\partial w_0}{\partial y}-M_1\mathrm{i}\gamma_3\right)\right]$$

$$\times\left.\left[\mathrm{i}\alpha_1\left(2u_{12}+2\frac{\partial u_0}{\partial y}-M_1\mathrm{i}\alpha_2\right)+\mathrm{i}\gamma_1\left(2w_{12}+2\frac{\partial w_0}{\partial y}-M_1\mathrm{i}\gamma_2\right)\right]\right\}$$

$$+(b-1)(b-3)|2V_0|^{b-5}\{2\mathrm{i}\alpha u_0+2\mathrm{i}\gamma w_0\}$$

$$\times\left\{2u_0\left(2u_{12}+2\frac{\partial u_0}{\partial y}-M_1\mathrm{i}\alpha_2\right)+2w_0\left(2w_{12}+2\frac{\partial w_0}{\partial y}-M_1\mathrm{i}\gamma_2\right)\right\}$$

$$\times\left\{2u_0\left(2u_{13}+2\frac{\partial u_0}{\partial y}-M_1\mathrm{i}\alpha_3\right)+2w_0\left(2w_{13}+2\frac{\partial w_0}{\partial y}-M_1\mathrm{i}\gamma_3\right)\right\}$$

$$+(b-1)|2V_0|^{b-3}\{2\mathrm{i}\alpha u_0+2\mathrm{i}\gamma w_0\}$$

$$\times\left\{\left[2u_{12}+2\frac{\partial u_0}{\partial y}-M_1\mathrm{i}\alpha_2\right]\left[2u_{13}+2\frac{\partial u_0}{\partial y}-M_1\mathrm{i}\alpha_3\right]\right.$$

$$+\left.\left[2w_{12}+2\frac{\partial w_0}{\partial y}-M_1\mathrm{i}\gamma_2\right]\left[2w_{13}+2\frac{\partial w_0}{\partial y}-M_1\mathrm{i}\gamma_3\right]\right\} \qquad (A\,2)$$

with

$$M_j = \frac{\mu R_d}{\Psi_{marg,j}}. \qquad (A\,3)$$

In all the above expressions the functions of y are evaluated at $y = \frac{1}{2}R_d/R_\delta$. We note that the expressions for b_2 and b_3 are similar to that for b_1 except for the following modifications. For b_2: replace M_1 with M_2, α_1 with α_2, α_2 with α_1, α_3 with $-\alpha_3$ and the same for the velocities: replace u_{12} with u_{11}, u_{13} with its complex conjugate $\bar{u}_{13}$, etc. Analogous modifications to (A\,2) hold for b_3.

REFERENCES

ALLEN, J. R. L. 1984 *Developments in Sedimentology*. Elsevier.

BLONDEAUX, P. 1990 Sand ripples under sea waves. Part 1. Ripple formation. *J. Fluid Mech.* **218**, 1–17.

BLONDEAUX, P., FOTI, E. & VITTORI, G. 2000 Migrating sea ripples. *Eur. J. Mech.* B/*Fluids*. **19**, 285–301.

COLOMBINI, M., SEMINARA, G. & TUBINO, M. 1987 Finite-amplitude alternate bars. *J. Fluid Mech.* **181**, 213–232.

CRAIK, A. D. D. 1971 Non-linear resonant instability in boundary layers. *J. Fluid Mech.* **50**, 393–413.

FREDSØE, J. 1974 On the developments of dunes on erodible channels. *J. Fluid Mech.* **64**, 1–16.

GRASS, J. A. & AYOUB, N. M. 1982 Bed load transport of fine sand by laminar and turbulent flow. *Proc 18th Coastal Engng Conf.* (ed. B. L. Edge), pp. 1589–1599. ASCE.

HARA, T. & MEI, C. C. 1990 Centrifugal instability of an oscillatory flow over periodic ripples. *J. Fluid Mech.* **217**, 1–32.

HSU, J. R. C., SILVESTER, R. & TSUCHIYA, Y. 1980 Boundary-layer velocities and mass transport in short-crested waves *J. Fluid Mech.* **99**, 321–342.

IRIE, I. & NADAOKA, K. 1984 Laboratory reproduction of seabed scour in front of breakwaters. *Proc. 19th Conf. on Coast. Engng, Reston, Va.*, vol. 2, pp. 1715–1731. ASCE.

JAN, C.-D. & LIN, M.-C. 1998 Bed forms generated on sandy bottom by oblique standing waves. *J. Waterway, Port, Coastal and Ocean Engng* **124**, 295–302.

MEI, C. C. 1989 *The Applied Dynamics of Ocean Surface Waves.* World Scientific.

ROOS, P. C. 2000 Sand ripples under sea waves. Tile ripples and other 3-D patterns. *Rep.* 06/00. Dept. Env. Engng, Universitá di Genova, pp. 39.

SCHIELEN, R., DOELMAN, A. & DE SWART, H. E. 1993 On the nonlinear dynamics of free bars in straight channels. *J. Fluid Mech.* **252**, 325–356.

SILVESTER, R. 1972 Wave reflection at seawalls and breakwaters. *Proc. Inst. Civil Engrs, Lond.* **51**, 123–131.

SILVESTER, R. 1975 Sediment transmission across entrances by natural means. *Proc. 16th Congress, IAHR*, vol. 1, pp. 145–156.

SLEATH, J. F. A. 1984 *Sea Bed Mechanics.* Wiley.

SLEATH, J. F. A. & ELLIS, A. C. 1978 Ripple geometry in oscillatory flow. *CUED/A-Hydraulics /*TR 2, University of Cambridge, Engineering Department.

STEGNER, A. & WESFREID, J. E. 1999 Dynamical evolution of sand ripples under water. *Phys. Rev. E.* **60**, 3487–3490.

STOKES, A. G. 1851 On the effect of internal friction of fluids on the motion of pendulums. *Trans. Camb. Phil. Soc.* **9**, 20–21.

VITTORI, G. 1992 Flow field induced by sea waves over brick-pattern ripples. *J. Hydr. Engng* **118**, 1241–1259.

VITTORI, G. & BLONDEAUX, P. 1990 Sand ripples under sea waves. Part 2. Finite amplitude development. *J. Fluid Mech.* **218**, 19–39.

VITTORI, G. & BLONDEAUX, P. 1992 Sand ripples under sea waves. Part 3. Brick-pattern ripple formation. *J. Fluid Mech.* **239**, 23–45.

VITTORI, G., DE SWART, H. E. & BLONDEAUX, P. 1999 Crescentic bedforms in the nearshore region. *J. Fluid Mech.* **381**, 271–303.